ADVANCED MATERIALS INTERFACES
www.advmatinterfaces.de

Biaxially Morphing Droplet Shape by an Active Surface

Ding Wang, Yingzhi Liu, Sreepathy Sridhar, Yifan Li, Glen McHale, Haibao Lu, Ziyi Yu, Steven Wang,* and Ben Bin Xu**

Drop morphology can be manipulated by designing localized solid/liquid interactions to create a favorable interfacial energy equilibrium. A topographical surface with hierarchical roughness can be harnessed to generate complex drop morphologies, enhance uniaxial and anisotropic spreading, in a designable fashion. Here, using an active surface is proposed with a responsive roughness (wrinkle patterns) under uniaxial compression/stretching, to morph droplet shape biaxially in a continuous and reversible manner. The keys to achieve biaxial drop shaping are the in-plane confinement from lattice hole patterns and the programmable formation of roughness, to pin and guide contact line movement in both in plane directions. The complex interplay between wetting and the patterns is elucidated by both experiments and numerical analysis. The results enrich the current understanding of shaping droplets by managing the contact line pinning/movement on an engineered elastic substrate, and providing insights for emerging applications in the areas such as droplet emicrofluidics, liquid robotics, ink-jet printing, 3D printing and healthcare.

Dr. D. Wang, Y. Liu, S. Sridhar, Dr. Y. Li, Prof. G. McHale, Prof. B. B. Xu
Smart Materials and Surfaces Laboratory
Faculty of Engineering and Environment
Northumbria University
Newcastle upon Tyne NE1 8ST, UK
E-mail: ben.xu@northumbria.ac.uk

Y. Liu, Prof. H. Lu
Science and Technology on Advanced Composites in Special Environments Laboratory
Harbin Institute of Technology
Harbin 150080, China

Prof. G. McHale
School of Engineering
University of Edinburgh
Edinburgh EH9 3JL, UK

Prof. Z. Yu
State Key Laboratory of Materials-Oriented Chemical Engineering
College of Chemical Engineering
Nanjing Tech University
Nanjing 211816, China
E-mail: ziyi.yu@njtech.edu.cn

Dr. S. Wang
Department of Mechanical Engineering
City University of Hong Kong
Hong Kong
E-mail: steven.wang@cityu.edu.hk

The ORCID identification number(s) for the author(s) of this article can be found under https://doi.org/10.1002/admi.202001199.

DOI: 10.1002/admi.202001199

Surfaces with controllable wetting properties are of great potential in downstream applications such as water harvesting,[1,2] self-cleaning,[3–5] surface coating,[6,7] adhesion[8–10] and microfluidic devices.[11–14] One strategy to facilitate controllable surface wetting is to develop surface topographies,[15–17] thereby enabling a desired liquid/solid interaction.[18–21] Recent advances have brought diverse approaches to create specific wetting performance by using chemical treatment,[22–24] dedicated pattern designs,[25–27] and functional materials.[28,29] Notably, Quéré and co-workers[16] manipulated the droplet shape on an elastic surface with soft pillars. Park and Kim used a shape memory polymer-based structure to shape droplets with adjustable surface morphology.[30] To date, the quest to achieve controllable surface wetting in a low cost, reliable and highly efficient fashion remains ongoing.

Recently, researchers developed strategies to control surface capillarity by creating surface wrinkles[31–33] and programmable surface roughness.[34–36] Designable wrinkle patterns with morphological transitions of periodicity, amplitude, and orientation under mechanical stimuli can enable a wetting anisotropy.[37–39] Some studies have investigated the wrinkling induced surface energy barriers and the associated contact line pinning. Stafford et al.[40] studied the wetting transitions upon a tunable single-period micro-wrinkled surfaces. Yang et al.[41] investigated the influences of wrinkle groove geometry on anisotropic wetting with a combining force balanced model. Feng et al.[42] reported anisotropic wetting on hierarchical wrinkled surfaces induced by curvature. Some of our authors explored the autonomous change of surface wetting by generating responsive wrinkle-cracking morphology on a gold/shape memory polymer bilayer.[43] However, the above studies focus on shaping droplets in one direction and the challenges on shaping a droplet bi-axially in a continuous, dynamic and reversible manner remain yet to be tackled.

In this work, we describe an approach to program a droplet from a circular shape to an ellipsoidal shape biaxially, upon a morphing surface consisting of a topographic lattice pattern and a stimuli-responsive roughness. Under uniaxial mechanical stimuli, localized wrinkle patterns can be initiated to create hierarchical structures on the surface selectively, yielding an enhanced pinning effect to pin and guide the movement of contact line. An analytical study is performed to understand the impact from surface geometries on droplet shaping. By varying

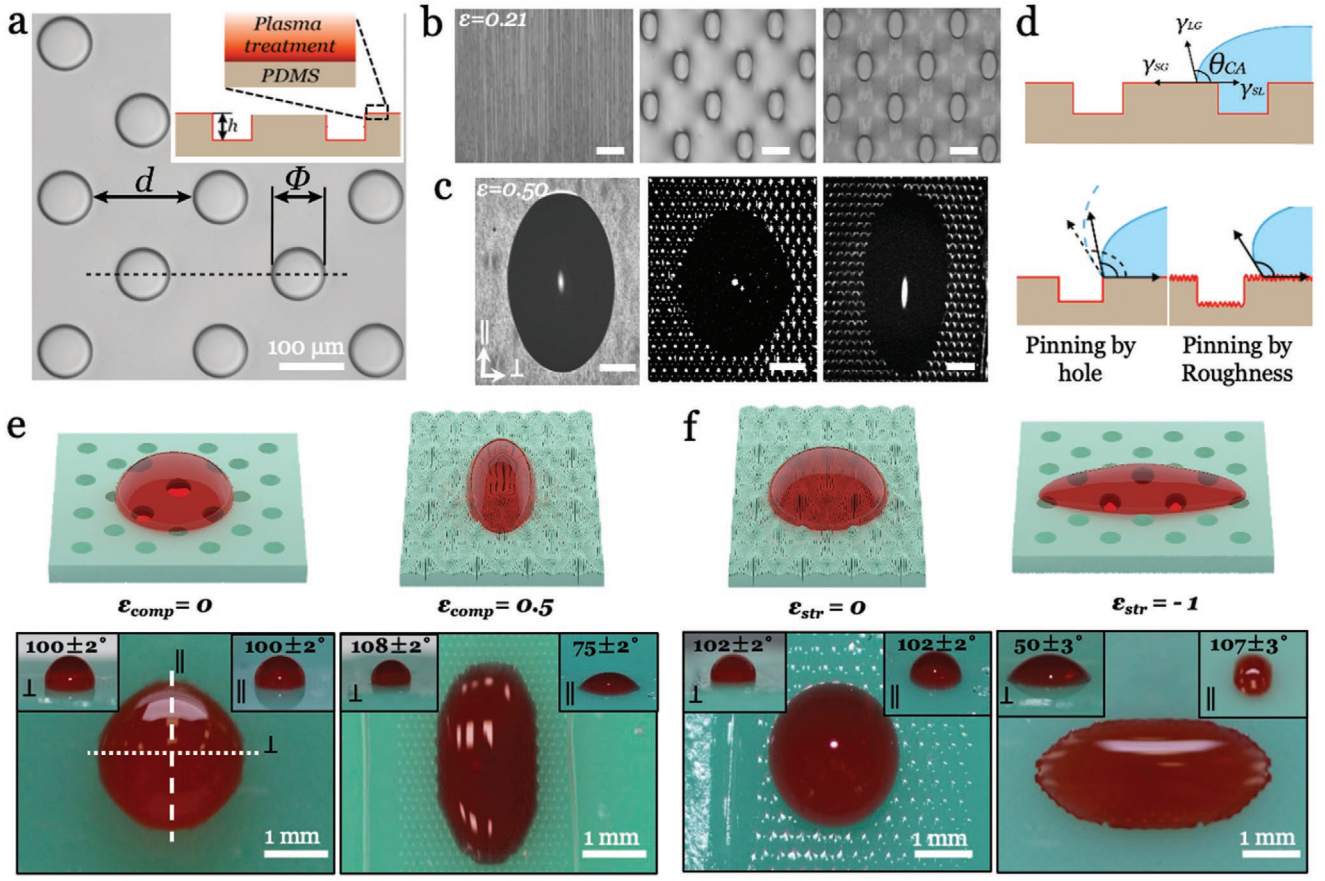

Figure 1. Surface design and realization of bi-axial shaping of droplet. a) Optical microscopic image of the patterned surface with lattice holes with the inset image to illustrate oxygen plasma treatment. b) Observations of surface morphologies at a uniaxial compressive strain (ε_{comp}) of 0.21 on plane surface after oxygen plasma treatment (left), patterned surface without oxygen plasma treatment (middle) and patterned surface with oxygen plasma treatment (right), c) Observation of droplet shaping at $\varepsilon_{comp} = 0.5$ for the corresponding surfaces in (b). d) The illustrations of local pinning effect on patterned surface and resulting contact angle changes. e) Schematic and illustration of shaping droplet under compression and f) stretching on patterned surface ($d = 160$ μm, $\Phi = 80$ μm, $h = 40$ μm). Unlabeled scale bars are 100 μm.

the geometrical factors for lattice patterns, we demonstrate that droplets can be morphed bi-axially in a reversible and continuous manner.

The structural elastic surface with a Bravais lattice pattern was prepared using the method previous reported by us,[44] the geometrical parameters, e.g. diameter (Φ), distance (d) and depth (h) are defined in **Figure 1**a. Oxygen plasma treatment was applied to create a stiff layer on the patterned soft substrate prior to the compression. By subsequently releasing the mounting layer from a pre-stretched length L_o to a length of L, the patterned surface is under uniaxial compression and the strain can be calculated by $\varepsilon_{comp} = 1 - L/L_o$. The wrinkling is observed for the plasma treated surfaces only (Figure 1b, $\varepsilon_{comp} = 0.21$). After depositing a droplet (2 μL) on the surface (Figure S1, Supporting Information), anisotropic wetting is realized (Figure 1c) for plain surface (Movie S1, Supporting Information), patterned surface without wrinkles (Movie S2, Supporting Information) and patterns surface with wrinkles (Movie S3, Supporting Information) under compression, where an elongated droplet with high aspect ratio oval shape is achieved by spreading along winkle patterns.[45–47] Directions perpendicular (⊥) and parallel (∥) to the wrinkle/groove direction are defined to describe surface topography and droplet shape (wetting anisotropy). Due to the pinning of contact line (Figure 1d), the contact angle (CA) perpendicular to groove appears larger than the parallel one.

Under uniaxial compression, surface instabilities occur and generate an additional energy barrier to resist the movement of liquid in the perpendicular direction (inset Figure 1e). Meanwhile, the droplet spreads along the parallel direction due to the absence of such a barrier. Consequently, an oval shape of droplet is generated with an aspect ratio ($D_{\parallel}/D_{\perp}$) of 1.87, where $D_{\parallel}$ and $D_{\perp}$ represent the diameter of droplet in the parallel and perpendicular directions, respectively. Programmable stretching of droplets is demonstrated by depositing a droplet on the fully compressed substrate with length L'_i, then gradually releasing the compressive strain to achieve the hole-open (initial) state (Figure 1f); the stretching strain ε_{str} is calculated by $\varepsilon_{str} = 1 - L/L'_i$. The continuous shaping of droplets is recorded for plain surface (Movie S4, Supporting Information), patterned surface without wrinkles (Movie S5, Supporting Information) and patterns surface with wrinkles (Movie S6, Supporting Information), the droplet reaches $D_{\parallel}/D_{\perp} \approx 0.45$ due to the pinning of contact line.

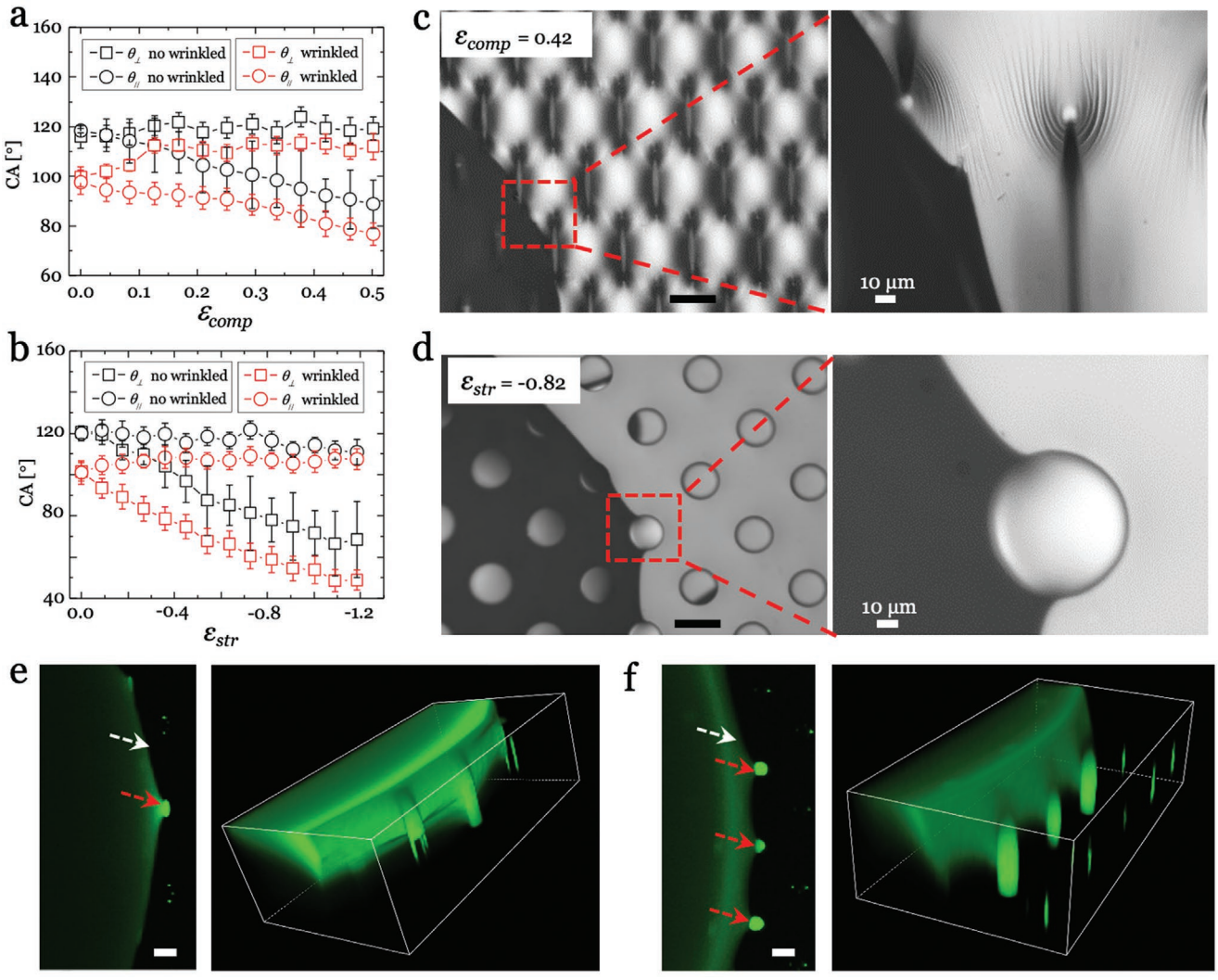

Figure 2. Tracking apparent contact angle (CA) bidirectionally and the change of contact line. Apparent CA in perpendicular (⊥) and parallel (||) directions from for a droplet on the wrinkled and un-wrinkled patterned surfaces (d = 160 μm, Φ = 80 μm, h = 40 μm), under continuous uni-axial a) compression and b) stretching. Observations of local pinning effects from c) wrinkles during the compression and d) pattern hole during the stretching. The top-view (left) and 3D reconstruction images (right) from laser confocal scanning microscopy to show contact line (white arrow) and wicking of pattern hole (red arrow) induced pinning effect during e) compression and f) stretching. Unlabeled error bars are 100 μm.

The apparent CAs are tracked to compare the impact from micropattern and hierarchical structure with wrinkles on the liquid/solid interface, during compression and stretching. For the lattice patterned surface without wrinkles, the apparent CA in the perpendicular direction ($\theta_{\perp}$, □) shows a value around 120° with an increasing trend (**Figure 2**a) under compression, however, the apparent CA in the parallel direction ($\theta_{\parallel}$, ◯) shows a declining trend in the parallel direction. For the lattice patterned surface with wrinkles, the apparent CA value reduces from 120° to 100° due to the plasma treatment. Compared with the lattice patterned surface without wrinkles, a large bifurcation of the CA values (≈45°) between the $\theta_{\perp}$ and $\theta_{\parallel}$ is obtained for the lattice patterned surface with wrinkles. Similar bifurcation trends in the apparent CA also appeared (Figure 2b) and a reduced deviation is observed to indicate the uniform regulation of CA during the stretching. A limited decrease for apparent CA (≈2.5°) is shown within 6 min as a result of evaporation (Figure S2, Supporting Information). With a stain rate of 0.04–0.004 s^{-1} and a saturation time of 5 s at each strain, the overall time for applying a compressive strain of 0.5 only takes less than 5 min, which allow the droplet to reach equilibrium at each step with ignorable system error from evaporation.

Moreover, we observe a strong pinning adhering to a wrinkled groove locally (Figure 2c) in the perpendicular direction under compression, where the curved edge of a droplet was forced to re-align to the straight line of wrinkle (Figure S3, Supporting Information). Under stretching, strong pinning effects arise from the hole in the parallel direction (Figure 2d), where the liquid tail is locally "dragged" by the curved edge of the hole due to the excess contact length. Further analysis from laser confocal scanning microscopic imaging (Figure 2e,f) suggests that wicking into the hole also creates localized contact line pinning, yielding to the shape changing of the droplet. The above monitoring identifies the anisotropic development of apparent

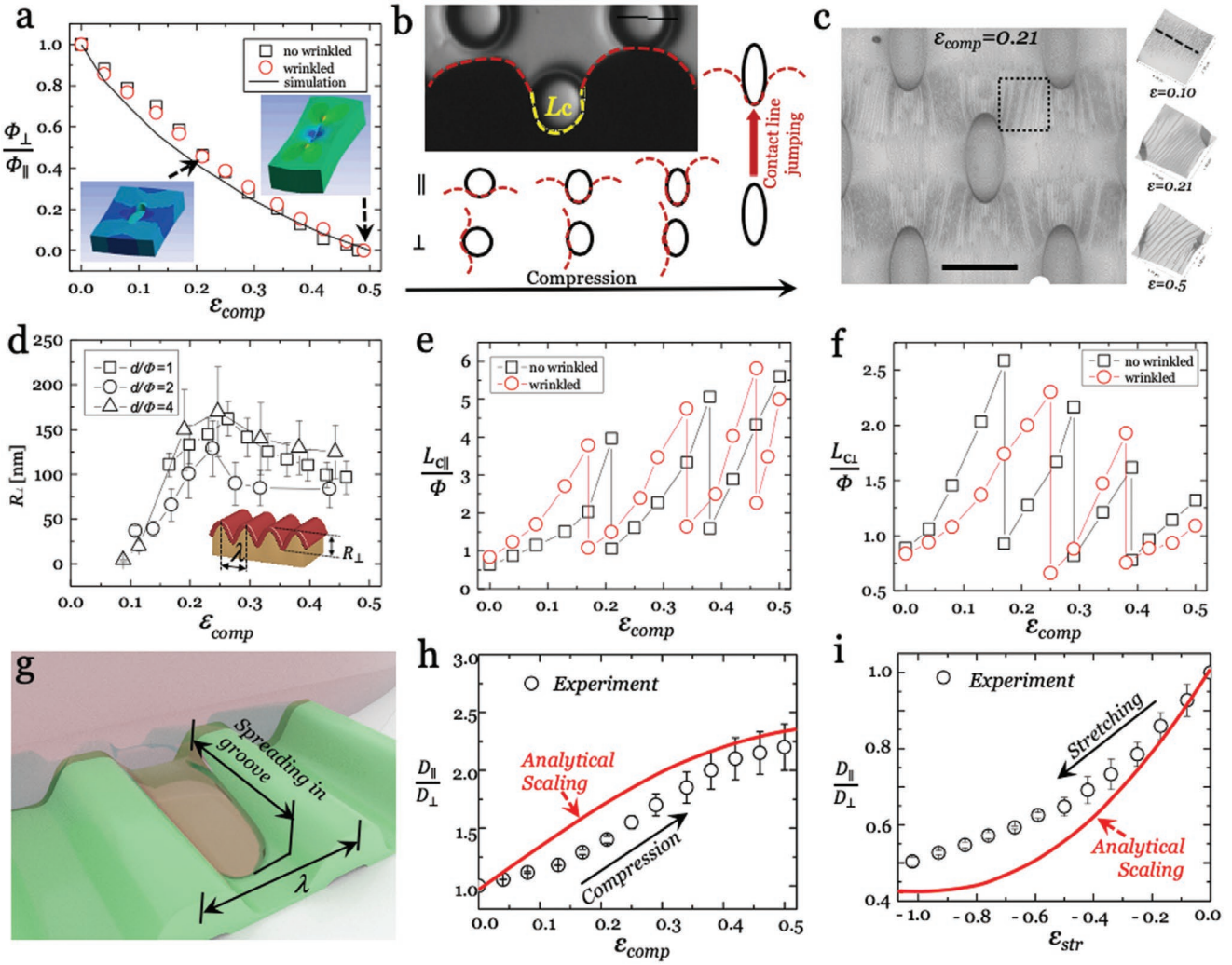

Figure 3. Surface structural analysis and its impact on contact line pinning. a) Experimental and FEA results of the elastic deformation of a unit substrate with single lattice hole under uniaxial compression. b) The pinning of contact line at the edge of a hole and the illustrations of dynamic progression of contact line at parallel (||) and perpendicular (⊥) directions under compression. c) Observation and AFM profiling of lattice patterned surface (d = 80 μm, Φ = 40 μm, h = 20 μm). d) Roughness ($R_\perp$) results for patterned surface of different pattern aspect ratio. The normalized pinning factor (L_c/Φ) as a function of ε_{comp} for the e) parallel and f) perpendicular directions. g) Schematic illustration of wrinkle guided wetting for droplet. Comparison of analytical with experimental data for h) compression and i) stretching.

CA occurs in perpendicular and parallel directions, which reshape the droplet. It should be noted that the above measurements were carried out by tracking a droplet under continuous uniaxial compression and stretching, therefore, the apparent CA reading deviates from a static equilibrium CA, due to the evaporation of liquid and local pinning effects.

Since the droplet is confined by the complex surface geometries crossing multiple length scales, e.g., the deformed edge of holes (up to hundreds of micrometers), wrinkles (nanometers to micrometers), etc, we then analyze the geometrical evolution on surface during compression and their impacts on solid/liquid interaction. The deformation of lattice holes is firstly studied (**Figure 3**a). A nonlinear deformation is unveiled for a single hole by finite element analysis (FEA) which reaches a full closure at around ε_{comp} = 0.5, where the experimental data also indicates a good agreement (ε_{comp} ≈ 0.48–0.49). There is limited mismatch between the wrinkled and no wrinkled curves since the energy to generate surface wrinkles is magnitude lower than that for deforming lattice hole. The deformation of hole will lead to subsequent changes of the in-plane energy barrier (Figure 3b), as the contact length is reduced in parallel and increased in perpendicular directions. We also analyze the generation of secondary roughness by tracing the surface morphological changes in a specific area (the dash box in Figure 3c) with AFM. For a patterned surface with aspect ratio d/Φ = 4 (Figure 3d, Δ), the measured roughness ($R_\perp$) is ≈50 nm at ε_{comp} = 0.13, followed by an increase to ≈170 mm at ε_{comp} = 0.21, then a gentle decrease until ε_{comp} = 0.46. The amplitude of wrinkle is predicted to be $R_\perp = h\,[\varepsilon/\varepsilon_c - 1]^{1/2}$,[43] or 58.49 nm at ε_{comp} = 0.13 for an oxidized layer thickness of 55 nm, which is in reasonable agreement with the measured value of ≈50 nm.

We then plot the normalized pinning factor (L_c/Φ) as a function of compressive strain to assess the directional restriction of contact line from lattice holes, where L_c refers to the length

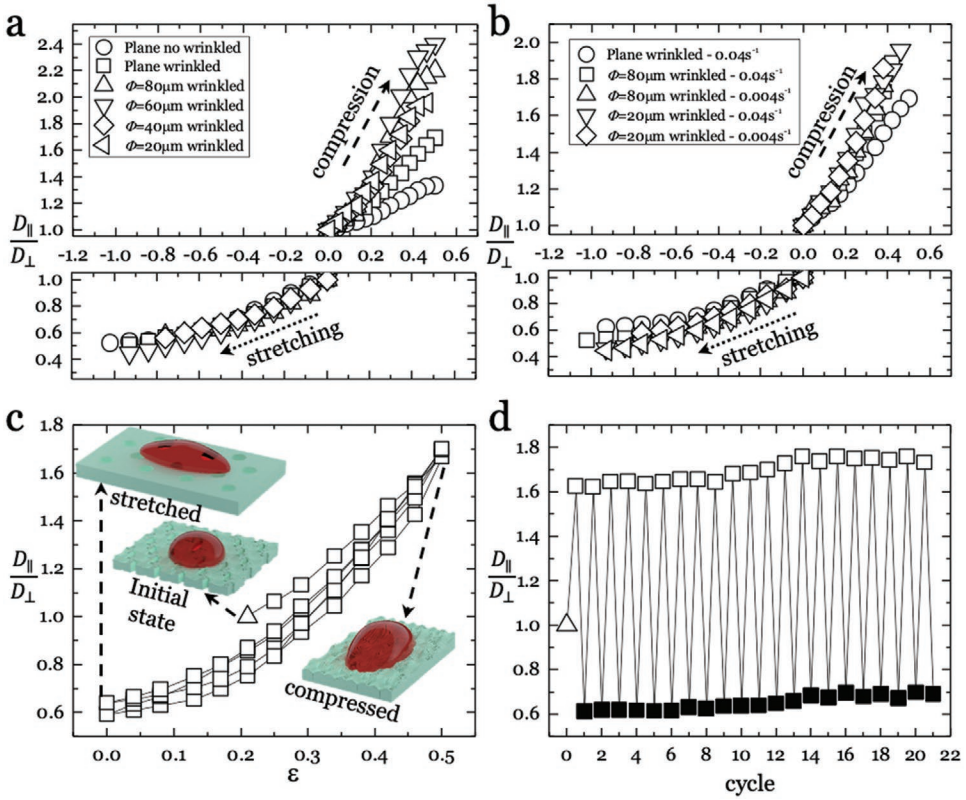

Figure 4. Evaluation of bi-axial droplet shaping and reproducibility. a) The effect of geometrical variations on shaping droplet. b) The effect of deforming speed on droplet shaping. c) the hysteresis for the biaxial droplet shaping. d) The cyclic droplet shaping for lattice patterned surface (d = 80 μm, Φ = 40 μm, h = 20 μm).

for a curved contact line around the hole (see Figure 3b). A slipping movement of contact line is discovered where the value of L_c/Φ initially increases with ε_{comp} increases (Figure 3e,f), then drops to a lower L_c/Φ for multiple times, which reflects the movement of contact line to overcome the energy barrier created by a lattice hole. It is found that the normalized pinning factors in parallel direction (Figure 3e) are higher than those for perpendicular direction (Figure 3f). Interestingly, we found that slip times of contact line for wrinkled surface are more than those without wrinkles in parallel direction, and a reversing trend in the perpendicular direction. The differential slipping of the contact line in two directions contribute to shaping the droplet, but the mechanism is unclear due to the development of complex surface, therefore, we defer this study as part of future work.

The directional dependence of standard static CA proves that the distribution of surface capillary has been tuned by the wrinkle induced roughness, where theoretical studies were previously demonstrated for various geometries.[48–50] The recent derivation of this square-law relationship by Khare et al.,[41] to predict the spread of water droplet on a wrinkled surface (Figure 3g) with the equation, $D^2(t)=\frac{\gamma}{8\pi\eta}\left[\left(\lambda+\frac{\pi^2A^2}{\lambda}\right)\cos\theta-\lambda\right]t$, where $D(t)$, the length of liquid along the parallel direction of wrinkle at a time t, shows the dependencies on the surface tension (γ) on the homogeneous PDMS surface, the viscosity (η) of the liquid, the contact angle (θ) and topographic properties (λ, A) of the substrate, and the slip-boundary condition. A similar analytical model can be developed to reveal the topographical effects on the droplet shaping along two axes with $D_{\parallel}^2(t)=\frac{\gamma}{8\pi\eta}\left[\left(\lambda+\frac{\pi^2A^2}{\lambda}\right)\cos\theta_{\parallel}-\lambda\right]t$ and $D_{\perp}^2(t)=\frac{\gamma}{8\pi\eta}[\lambda\cos\theta_{\perp}-\lambda]t$, since the amplitude ($A$) will be around zero in calculating $D_{\perp}$.

By combining above equations, we can obtain the analytical model for aspect ratio of droplet shape under compression as $\frac{D_{\parallel}}{D_{\perp}}=\left[\frac{\left(1+\frac{\pi^2A^2}{\lambda^2}\right)\cos\theta_{\parallel}-1}{\cos\theta_{\perp}-1}\right]^{1/2}$. For stretching, a similar equation can be derived as $\frac{D_{\parallel}}{D_{\perp}}=\left[\frac{\cos\theta_{\parallel}-1}{\left(1+\frac{\pi^2A^2}{\lambda^2}\right)\cos\theta_{\perp}-1}\right]^{1/2}$. The standard static CA (Figure S4, Supporting Information) were used in this calculation which were obtained by depositing droplets on the deformed surface at each strain, to avoid the deviations in Figure 2a,b. We use the geometrical input of A/λ in previous publication[44] to create the scaling. By comparing the analytical results with the experimental data, a good agreement is found for compression (Figure 3h), while there are considerable gaps for stretching (Figure 3i), probably due to the wicking on lattice holes reduce the overall droplet volume thus leading to the receding of contact line globally.

The impact from geometrical factors of lattice pattern (hole size) on droplet shaping is studied under compression (positive strain) and stretching (negative strain) (**Figure 4**a).

Under compression, wetting anisotropy on the plane surface (non-patterned and no wrinkles) gives a value of $D_{\parallel}/D_{\perp} = 1.3$ for the droplet, whereas the plane surface with wrinkles achieves a $D_{\parallel}/D_{\perp}$ of 1.6. The quantitative results indicate that the lattice patterned surfaces with wrinkle reaches a significant increase in wet anisotropy with values of $D_{\parallel}/D_{\perp}$ high than 1.8, even achieving a peak value of $D_{\parallel}/D_{\perp} = 2.4$ for the patterned surface with a hole diameter of 60 µm. Under stretching, all lattice patterned surfaces (wrinkled and non-wrinkled) present low $D_{\parallel}/D_{\perp}$ values of around 0.45, indicating a better shaping effect than the plane surface (non-patterned and no wrinkles) which has a $D_{\parallel}/D_{\perp}$ of 0.55.

We next assess the droplet shaping performance as function of loading/unloading rate for different surfaces (Figure 4b). With increasing average strain rates over the range of 0.004–0.04 s^{-1}, the results suggest limited difference at compression and stretching for the surface patterned with same lattice array. One key advantage of using this elastic process to achieve anisotropic wetting, is the reversibility and high repeatability. We measure the uniaxial shaping of droplet and a robust performance is observed in three loops (Figure S5, Supporting Information). The biaxial shaping of droplet was performed by depositing the droplet on the substrate with partially relieving the prestrain of substrate to 0.2 (Figure 4c). From Figure 4c, a hysteresis for $D_{\parallel}/D_{\perp}$ is found less than 0.1 between the first compression and the second cycle. From the second cycle, the hysteresis become ignorable. The robust biaxial droplet shaping upon the structural elastic surface is obtained (Figure 4d), with high $D_{\parallel}/D_{\perp}$ values between 1.65 to 1.7 and low $D_{\parallel}/D_{\perp}$ values from 0.65 to 0.77 over multiple cycles. We also notice a small increase on both values, probably due to the relaxation of substrate, the viscoelastic nature of interaction between the substrate and droplet, and/or the development hydroxyl groups surface.

The biaxial shaping of droplets is achieved on an active surface, which is functionalized by a topographical lattice pattern with a responsive roughness activated by uniaxial mechanical deformation. This dynamic shaping of droplet is driven by the pinning and guided movement of the contact line of the liquid. We investigate the effects from the pattern deformation and the localized transformative wrinkle grooves on the interplay between liquid and solid along two axes. Numerical analysis is performed to understand the impact of wrinkle geometries on the shape changes for a droplet, which agree well with the experimental results. We demonstrate continuous and reversible morphing of the droplet shape biaxially. The directional transitions of this anisotropic wetting enrich the physical picture of the interface of liquid/elastic topographical solids, and will be expected to bring advantages in emerging applications in droplet microfluidic, self-cleaning, liquid robotics, inkjet printing, 3D printing, water treatment, healthcare, etc.

Experimental Section

Fabrication of Structural Elastic Bilayer: Structural patterned templates of SU-8 micropillar on silicon wafer were fabricated by standard photolithography. First of all, a mounting layer was made from vinylpolysiloxane (VPS) elastomer (Elite Double 22, Zhermack Ltd). The VPS was created by mixing a base with curing agent at a weight ratio of 1:1, the mixture was then cured in petri dish at room temperature for 1 h. The thickness of cured VPS film was about 3 mm, and a rectangular stripe of 9 mm × 30 mm was cut and uniaxially pre-stretched to 600% of its original length on a mechanical vice. A self-assembled monolayer (SAM) of trichloro (1H, 1H, 2H, 2H-perfluorooctyl) silane (Sigma-Aldrich) was applied via a vapor-phase procedure at room temperature for 15 min to facilitate subsequent releasing of PDMS film from SU-8 template. The soft PDMS layer with thickness of 125 µm (Sylgard 184, Dow Corning, 30:1 for elastomer base: crosslinker) was prepared by spin-coating the degassed mixture on a SU-8 patterned silicon wafer (≈1 cm^2) at 1000 rpm for 120 s, followed by curing at 70 °C for 1 h. An adhesive PDMS layer with the same composition of 30:1 was spin-coated on this cured layer at 3000 rpm for 120 s, to bond to the VPS mounting layer. After transferring the adhesive coated soft PDMS layer to the mounting layer, the assembly was cured at 70 °C for 8 h. Prior to characterization, the structured PDMS surface was treated by oxygen plasma (HPT-100, Henniker) at a working power of 100 W, under a mixed gas atmosphere of oxygen/nitrogen ratio ≈ 0.2.

Characterization: The experiment was carried out immediately after the oxygen plasma treatment. A 2 µL deionized (DI) water droplet (dyed with red food color gel, Dr. Oetker, at a weight ratio of 10:1) was deposited on the sample surface using a micropipette. Deformation strains were incrementally applied by releasing the pre-stretched VPS mounting layer (Elite Double 22, Zhermack Ltd) at regular intervals with a rate of 0.004–0.04 s^{-1}. A saturation time of 5 s are left before taking each observation. 2D profiles of the droplet was recorded in situ using both an upright optical microscope (Nikon LV-100) in brightfield reflection mode and a digital camera (model D3200, Nikon) with a macro lens (model 105 mm 1:2.8, SIGMA). Standard static contact angle (CA), advancing CA and receding CA value of droplet were measured using a Droplet Shape Analyzer (DSA30S, Kruss) by following the standard process to capture the droplet shape at the equilibrium. The surface topographic features were assessed with an atom force microscopy (D3100, Veeco). Laser scanning confocal fluorescence microscopy (Nikon A1R) was used to observe the droplet shape in 3D with Fluorescein isothiocyanate-dextran (SIGMA) as dye at a weight ratio of 1000:1 for DI water: dye.

Finite Element Simulations: Finite element simulations were conducted using the commercial simulation package–ABAQUS. An incompressible Neo-Hookean material model was used under plane-strain conditions. An isotropic, uniform strain deformation was applied to match the typical level of deformation in the experimental system. The Explicit Dynamic solver was used in the simulation.

Supporting Information

Supporting Information is available from the Wiley Online Library or from the author.

Acknowledgements

D.W. and Y.L. contributed equally to this work. The work was supported by the Engineering and Physical Sciences Research Council (EPSRC) grant-EP/N007921 and EP/L026899, Royal Society research grant-RG150662 and Kan Tong Po International Fellowship 2019-KTP\R1\191012. D.W. and B.B.X. thank Reece Innovation for the studentship support.

Conflict of Interest

The authors declare no conflict of interest.

Keywords

droplet shaping, elastic instability, surface wetting, wrinkling

Received: July 2, 2020
Revised: July 27, 2020
Published online:

[1] M. Faustini, A. Cattoni, J. Peron, C. Boissière, P. Ebrard, A. Malchère, P. Steyer, D. Grosso, *ACS Nano* **2018**, *12*, 3243.
[2] Y. Y. Song, Y. Liu, H. B. Jiang, S. Y. Li, C. Kaya, T. Stegmaier, Z. W. Han, L. Q. Ren, *Nanoscale* **2018**, *10*, 16127.
[3] A. Vanangamudi, L. F. Dumée, E. Des Ligneris, M. Duke, X. Yang, *J. Membr. Sci.* **2019**, *574*, 309.
[4] A. Sabbah, A. Youssef, P. Damman, *Appl. Sci.* **2016**, *6*, 152.
[5] M. R. Esfahani, N. Koutahzadeh, A. R. Esfahani, M. D. Firouzjaei, B. Anderson, L. Peck, *J. Membr. Sci.* **2019**, *573*, 309.
[6] K.-M. Lee, H. Park, J. Kim, D.-M. Chun, *Appl. Surf. Sci.* **2019**, *467-468*, 979.
[7] X. Deng, L. Mammen, H.-J. Butt, D. Vollmer, *Science* **2012**, *335*, 67.
[8] D. Quéré, *Annu. Rev. Mater. Res.* **2008**, *38*, 71.
[9] L. Pocivavsek, J. Pugar, R. O. Dea, S. Ye, W. Wagner, E. Tzeng, S. Velankar, E. Cerda, *Nat. Phys.* **2018**, *14*, 948.
[10] U. U. Ghosh, S. Nair, A. Das, R. Mukherjee, S. DasGupta, *Colloids Surf., A* **2019**, *561*, 9.
[11] C.-H. Choi, H. Lee, D. A. Weitz, *ACS Appl. Mater. Interfaces* **2018**, *10*, 3170.
[12] Y. Yang, L. Zhang, J. Wang, X. Wang, L. Duan, N. Wang, F. Xiao, Y. Xie, J. Zhao, *ACS Appl. Mater. Interfaces* **2018**, *10*, 19182.
[13] P. Estellé, D. Cabaleiro, G. Żyła, L. Lugo, S. M. S. Murshed, *Renewable Sustainable Energy Rev.* **2018**, *94*, 931.
[14] C. Yang, L. Wu, G. Li, *ACS Appl. Mater. Interfaces* **2018**, *10*, 20150.
[15] H. Kusumaatmaja, R. J. Vrancken, C. W. M. Bastiaansen, J. M. Yeomans, *Langmuir* **2008**, *24*, 7299.
[16] M. Coux, C. Clanet, D. Quéré, *Appl. Phys. Lett.* **2017**, *110*, 251605.
[17] D. Rhee, W. K. Lee, T. W. Odom, *Angew. Chem., Int. Ed.* **2017**, *56*, 6523.
[18] S. Adera, R. Raj, R. Enright, E. N. Wang, *Nat. Commun.* **2013**, *4*, 2518.
[19] R. Raj, S. Adera, R. Enright, E. N. Wang, *Nat. Commun.* **2014**, *5*, 4975.
[20] Q. Yuan, Y. P. Zhao, *Sci. Rep.* **2013**, *3*, 3.
[21] S. Chung, J. H. Lee, M.-W. Moon, J. Han, R. D. Kamm, *Adv. Mater.* **2008**, *20*, 3011.
[22] S. Chatterjee, K. Pal Singh, S. Bhattacharjee, *Appl. Surf. Sci.* **2019**, *470*, 773.
[23] Y. L. Tian, Y. C. Zhao, C. J. Yang, F. J. Wang, X. P. Liu, X. B. Jing, *J. Colloid Interface Sci.* **2018**, *527*, 328.
[24] Ç. K. Söz, S. Trosien, M. Biesalski, *ACS Appl. Mater. Interfaces* **2018**, *10*, 37478.
[25] H. Han, J. S. Lee, H. Kim, S. Shin, J. Lee, J. Kim, X. Hou, S.-W. Cho, J. Seo, T. Lee, *ACS Nano* **2018**, *12*, 932.
[26] N. A. Malvadkar, M. J. Hancock, K. Sekeroglu, W. J. Dressick, M. C. Demirel, *Nat. Mater.* **2010**, *9*, 1023.
[27] P. Wang, R. Bian, Q. Meng, H. Liu, L. Jiang, *Adv. Mater.* **2017**, *29*, 1703042.
[28] P. Ge, J. Zhang, Y. Liu, S. Wang, W. Liu, N. Yu, Y. Wu, J. Zhang, B. Yang, *Adv. Funct. Mater.* **2018**, *28*, 1802001.
[29] Z. Cheng, D. Zhang, T. Lv, H. Lai, E. Zhang, H. Kang, Y. Wang, P. Liu, Y. Liu, Y. Du, S. Dou, L. Jiang, *Adv. Funct. Mater.* **2018**, *28*, 1705002.
[30] J. K. Park, S. Kim, *Lab Chip* **2017**, *17*, 1793.
[31] M. C. Giordano, F. B. de Mongeot, *Adv. Mater.* **2018**, *30*, 1801840.
[32] S. Zeng, R. Li, S. G. Freire, V. M. M. Garbellotto, E. Y. Huang, A. T. Smith, C. Hu, W. R. T. Tait, Z. Bian, G. Zheng, D. Zhang, L. Sun, *Adv. Mater.* **2017**, *29*, 1700828.
[33] G. Lin, Q. Zhang, C. Lv, Y. Tang, J. Yin, *Soft Matter* **2018**, *14*, 1517.
[34] T.-H. Chang, T. Zhang, H. Yang, K. Li, Y. Tian, J. Y. Lee, P.-Y. Chen, *ACS Nano* **2018**, *12*, 8048.
[35] E. Cerda, L. Mahadevan, *Phys. Rev. Lett.* **2003**, *90*, 74302.
[36] Y. Wang, Q. Liu, J. Zhang, T. Hong, W. Sun, L. Tang, E. Arnold, Z. Suo, W. Hong, Z. Ren, C. F. Guo, *Adv. Mater.* **2019**, *31*, 1902955.
[37] W.-K. Lee, W.-B. Jung, D. Rhee, J. Hu, Y.-A. L. Lee, C. Jacobson, H.-T. Jung, T. W. Odom, *Adv. Mater.* **2018**, *30*, 1706657.
[38] E. P. Chan, E. J. Smith, R. C. Hayward, A. J. Crosby, *Adv. Mater.* **2008**, *20*, 711.
[39] S. Peppou-Chapman, C. Neto, *ACS Appl. Mater. Interfaces* **2018**, *10*, 33669.
[40] J. Y. Chung, J. P. Youngblood, C. M. Stafford, *Soft Matter* **2007**, *3*, 1163.
[41] K. Khare, J. Zhou, S. Yang, *Langmuir* **2009**, *25*, 12794.
[42] Z. C. Shao, Y. Zhao, W. Zhang, Y. Cao, X. Q. Feng, *Soft Matter* **2016**, *12*, 7977.
[43] H. Lu, Y. Liu, B. B. Xu, D. Hui, Y. Q. Fu, *Composites, Part B* **2017**, *122*, 9.
[44] D. Wang, N. Cheewaruangroj, Y. Li, G. McHale, Y. Jiang, D. Wood, J. S. Biggins, B. B. Xu, *Adv. Funct. Mater.* **2018**, *28*, 1704228.
[45] D. Xia, S. R. J. Brueck, *Nano Lett.* **2008**, *8*, 2819.
[46] D. Xia, X. He, Y.-B. Jiang, G. P. Lopez, S. R. J. Brueck, *Langmuir* **2010**, *26*, 2700.
[47] C. Semprebon, C. Herrmann, B. Y. Liu, R. Seemann, M. Brinkmann, *Langmuir* **2018**, *34*, 10498.
[48] W. Gardner, *Phys. Rev.* **1921**, *18*, 206.
[49] J. C. Baret, M. M. J. Decré, S. Herminghaus, R. Seemann, *Langmuir* **2007**, *23*, 5200.
[50] R. R. Rye, J. A. Mann, F. G. Yost, *Langmuir* **1996**, *12*, 555.